nature computational science

ARTICLES

https://doi.org/10.1038/s43588-021-00157-1

How connectivity rules and synaptic properties shape the efficacy of pattern separation in the entorhinal cortex–dentate gyrus–CA3 network

S. Jose Guzman[1,2], Alois Schlögl[1], Claudia Espinoza[1,3], Xiaomin Zhang[1,4], Benjamin A. Suter[1] and Peter Jonas[1]✉

Pattern separation is a fundamental brain computation that converts small differences in input patterns into large differences in output patterns. Several synaptic mechanisms of pattern separation have been proposed, including code expansion, inhibition and plasticity; however, which of these mechanisms play a role in the entorhinal cortex (EC)–dentate gyrus (DG)–CA3 circuit, a classical pattern separation circuit, remains unclear. Here we show that a biologically realistic, full-scale EC–DG–CA3 circuit model, including granule cells (GCs) and parvalbumin-positive inhibitory interneurons (PV$^+$-INs) in the DG, is an efficient pattern separator. Both external gamma-modulated inhibition and internal lateral inhibition mediated by PV$^+$-INs substantially contributed to pattern separation. Both local connectivity and fast signaling at GC–PV$^+$-IN synapses were important for maximum effectiveness. Similarly, mossy fiber synapses with conditional detonator properties contributed to pattern separation. By contrast, perforant path synapses with Hebbian synaptic plasticity and direct EC–CA3 connection shifted the network towards pattern completion. Our results demonstrate that the specific properties of cells and synapses optimize higher-order computations in biological networks and might be useful to improve the deep learning capabilities of technical networks.

A fundamental question in neuroscience is how higher-order computations are implemented at the level of synapses, neurons and neuronal networks. A key computation in the brain is pattern separation, a process that converts slightly different synaptic input patterns into substantially different action potential output patterns[1–4]. Although pattern separation is a universal network computation conserved across circuits and species[4], it is thought to play a particularly important role in the dentate gyrus (DG), the input region of the hippocampus in mammals[5,6]. A prevalent model of hippocampal memory suggests that pattern separation in the DG is essential for reliable storage and recall of memories in the downstream CA3 region[2,7,8]. Thus, analyzing the mechanisms of pattern separation is crucial for the understanding of both short-term processing and long-term storage of information.

Early models of pattern separation, inspired by the architecture of the cerebellum[4,9,10], suggested that divergent feedforward excitation and code expansion play a role in pattern separation[9]. According to the Marr–Albus theory, projection from a small to a large population of neurons expands the dimensionality of coding space, increasing the separability of patterns by downstream biological decoders[10]. The Marr–Albus model is consistent with structural and functional connectivity rules of the cerebellum, as a single mossy fiber axon divergently projects onto ~600 granule cells (GCs)[4]. Whether code expansion also explains pattern separation in the rodent hippocampus, where ~50,000 entorhinal cortex (EC) neurons diverge to ~500,000 GCs, which reconverge onto ~200,000 CA3 pyramidal neurons[11–13], is an open question.

More recent models of pattern separation implied an important role of lateral inhibition[14]. These models were supported by the synaptic organization of the olfactory system in insects[15–17]. In the mushroom body of the fly, a single inhibitory cell, the anterior paired lateral (APL) interneuron, plays a role in pattern separation. Activation of a single Kenyon cell activates the APL interneuron, which in turn provides powerful inhibition to all Kenyon cells[16]. Thus, global lateral inhibition mediated by the APL interneuron could implement a winner-takes-all mechanism, thereby establishing a powerful decorrelation algorithm[18–20]. Whether inhibition contributes to pattern separation in the DG is less clear. Although lateral inhibition is uniquely abundant in the DG, multiple GCs need to fire action potentials to activate parvalbumin-positive inhibitory interneurons (PV$^+$-INs) and to trigger lateral inhibition[21,22]. Furthermore, lateral inhibition is not global, but follows distance-dependent connectivity rules[22]. Thus, lateral inhibition cannot implement a winner-takes-all mechanism, although softer versions with multiple winners remain possible[18,19,23].

The DG is connected to the downstream CA3 region via powerful mossy fiber synapses[2,7]. Whereas the DG seems to be specialized on pattern separation, the CA3 region is traditionally associated with pattern completion[8,24]. How the pattern separation mechanism in the DG is integrated with the pattern completion function of the CA3 region remains enigmatic. Furthermore, how the unique properties of hippocampal mossy fiber synapses, such as conditional and plasticity-dependent detonation[25], contribute to pattern separation is unclear. Detonation properties of mossy fiber synapses may facilitate the transfer of information from the DG to CA3 region, which might contribute to pattern separation[23]. Furthermore, sparse mossy fiber connectivity will reduce correlations, which may enhance pattern separation[26]. Whether these rules hold in biologically realistic network models remains to be determined.

[1]IST Austria, Klosterneuburg, Austria. [2]Present address: Institute of Molecular Biotechnology, Vienna, Austria. [3]Present address: Medical University of Austria, Division of Cognitive Neurobiology, Vienna, Austria. [4]Present address: Brain Research Institute, University of Zürich, Zurich, Switzerland. ✉e-mail: Peter.Jonas@ist.ac.at

The DG receives its main input from the EC via the perforant path (PP)[27]. Hebbian plasticity at PP synapses could implement a competitive learning mechanism[2,28,29], which might contribute to pattern separation. Consistent with this idea, genetic deletion of *N*-methyl-D-aspartate (NMDA)-type glutamate receptors in GCs reduces behavioral pattern separation[30]. However, plasticity at PP EC–GC synapses has also been suggested to contribute to pattern completion[8,31]. As an additional complication, the PP not only projects to GCs in the DG, but also directly innervates the CA3 region[32]. In a simplified model, the relative strength of the mossy fiber and PP input onto CA3 pyramidal neurons determines the balance between decorrelated and original input[23]. However, whether this is also the case in a biologically realistic model remains unclear.

We developed a model based on experimentally determined cellular and synaptic properties to address the mechanisms of pattern separation in the EC–DG–CA3 network. Implementation in real size allowed us to analyze sparse coding regimes[33] and to insert measured connectivity rules[22].

Results

Pattern separation in a biologically realistic PN–IN network. Pattern separation is a fundamental brain computation that converts small differences in input patterns into large differences in output patterns. The basic principle is illustrated in Extended Data Fig. 1. When two highly overlapping patterns (A and B) are applied at the input level of a neuronal population, two less overlapping patterns (A′ and B′) are generated at the output level (Extended Data Fig. 1a). Quantitatively, for any given pair of patterns, the correlation r at the output ($R_{out} = r(A', B')$) is smaller than that at the input ($R_{in} = r(A, B)$) (Extended Data Fig. 1b). Thus, pattern separation may be graphically depicted in a plot of R_{out} against R_{in} for all pairs of patterns[23]. For an efficient pattern separation mechanism, the data points would be expected to be located below the identity line (Extended Data Fig. 1c). By contrast, for a pattern completion mechanism[8], the data points will be above the identity line (Extended Data Fig. 1d).

We used three different measures to quantify the properties of the pattern separation circuit (Methods). First, to describe the overall pattern-separation performance, we defined an integral-based measure, ψ, computed as the area between the R_{out}–R_{in} data and the identity line, normalized by the maximal area (Extended Data Fig. 1e). Second, to selectively capture pattern separation performance within a region in which input patterns were highly similar, we defined a slope-based measure, γ, computed as the slope of the R_{out}–R_{in} curve for $R_{in} \rightarrow 1$ (Extended Data Fig. 1e, inset). Finally, to characterize the ability of the network to preserve rank similarity[34–36], we computed a rank-based correlation coefficient ρ (Extended Data Fig. 1f). These three parameters describe complementary aspects of pattern separation. For example, randomization is well known to decorrelate patterns (increasing the values of ψ and γ), but fails to maintain similarity relations (decreasing the value of ρ).

To explore whether a biologically realistic network is capable of pattern separation, we developed a model of the EC–DG–CA3 network based on empirical experimental data (Fig. 1; Supplementary Fig. 1; Supplementary Table 1; Supplementary Software). The network was created in full scale[12,13]. Both principal neuron–interneuron (PN–IN) connectivity in the DG and GC–CA3 connectivity was constrained by experimental data[21,22,37]. Similarly, GC–CA3 connectivity via mossy fibers was experimentally constrained[11,25,38–40]. As gamma oscillations show maximal power in the DG[41,42], a corresponding phasic inhibitory conductance was simulated in GCs at the onset of each simulation epoch[19]. The model allowed us to simulate the activity in GCs, PV^+-INs and CA3 pyramidal neurons in a biologically realistic network, and to examine how biophysical properties of synapses and functional connectivity rules affect pattern separation (Fig. 1b).

Pattern separation by gamma rhythm and lateral inhibition. The finding that pattern separation accumulated in a multilayer deep network-like architecture was surprising, given that the divergence–convergence properties of the circuit seemed inconsistent with a code-expansion model[9,10]. We examined the contribution of inhibition to explore alternative mechanisms of pattern separation (Fig. 2)[4,9]. It has been suggested that both external gamma-modulated inhibition and internal lateral inhibition contribute to pattern separation[14,18,19,43,44]. We therefore explored gamma-modulated and lateral inhibition (in isolation as well as in combination) for a suprathreshold excitatory drive to GCs ($I_\mu = 1.8$ relative to threshold). Deletion of gamma-modulated external inhibition from the network model ($J_{gamma} = 0$) reduced ψ and γ over a wide excitatory synaptic drive range (Fig. 2b, top right). By contrast, deletion of lateral inhibition reduced the excitatory drive range in which both high ψ and ρ could be achieved (Fig. 2b, bottom left); thus, gamma inhibition and lateral inhibition differentially affected pattern separation. Elimination of both forms of inhibition substantially impaired pattern separation (Fig. 2b, bottom right) and therefore the combination of gamma-modulated inhibition and lateral inhibition provides a major contribution to separation mechanism in the model. To further analyze the complex interaction of tonic excitatory drive, gamma-modulated inhibition and lateral inhibition, we computed ψ–I_μ–J_{gamma} contour plots (Fig. 2c,d). With intact lateral inhibition, efficient pattern separation ($\psi > 0.5$) was robustly observed in a wide region of the parameter space (Fig. 2c). By contrast, after deletion of lateral inhibition, efficient pattern separation was only detected within a narrow band in the I_μ–J_{gamma} parameter space, in which the amplitude of gamma-modulated inhibition precisely matched that of the excitatory drive (Fig. 2d); thus, a simple thresholding mechanism combined with gamma-modulated inhibition was not sufficient to generate robust pattern separation.

Finally, we explored how interfering with lateral inhibition at multiple levels affects pattern separation (Fig. 2e–g). Reducing the peak connectivity of either excitatory E–I or inhibitory I–E connections (c_{E-I} and c_{I-E}, respectively) markedly affected the efficacy of pattern separation (Fig. 2e, light blue bars). Similarly, reducing the connectivity width of either excitatory E–I or inhibitory I–E connections (σ_{E-I} and σ_{I-E}, respectively) reduced the efficacy of pattern separation (Fig. 2f). Finally, reducing the strength of either excitatory E–I or inhibitory I–E connections (J_{E-I} or J_{I-E}, respectively) substantially decreased the efficacy of pattern separation (Fig. 2g); thus, interfering with disynaptic inhibition at multiple levels uniformly inhibited pattern separation. Taken together, the combination of gamma oscillations and lateral inhibition plays a critical role in the pattern separation process in the DG.

Moderate effects of divergent connectivity. To systematically explore how divergence and convergence affect pattern separation, we first examined pattern separation in simple models, in which convergent or divergent connectivity was concatenated with a thresholding mechanism (Fig. 3a–d). In this simple model, the number of neurons and the degree of convergence and divergence could be freely varied. In our simulations, we changed the connectivity ratio from 1:10 (divergence) to 10:1 (convergence). In contrast to our expectations, the degree of pattern separation, as quantified by ψ, was only slightly dependent on the connectivity ratio (Fig. 3c,d). Weak dependence on the connectivity ratio was observed over a wide range of activity values (Fig. 3d); thus, divergent connectivity was not strictly required for pattern separation.

We next determined how convergence and divergence affected pattern separation in the full-scale, biologically realistic network model (Fig. 3e–g). To address this aspect, we varied the number or activity level of entorhinal cells (n_{EC} or α_{EC}, respectively), and the peak value or width of EC-GC connectivity[27,32,45]. Increasing the number of ECs decreased ψ, whereas decreasing the number

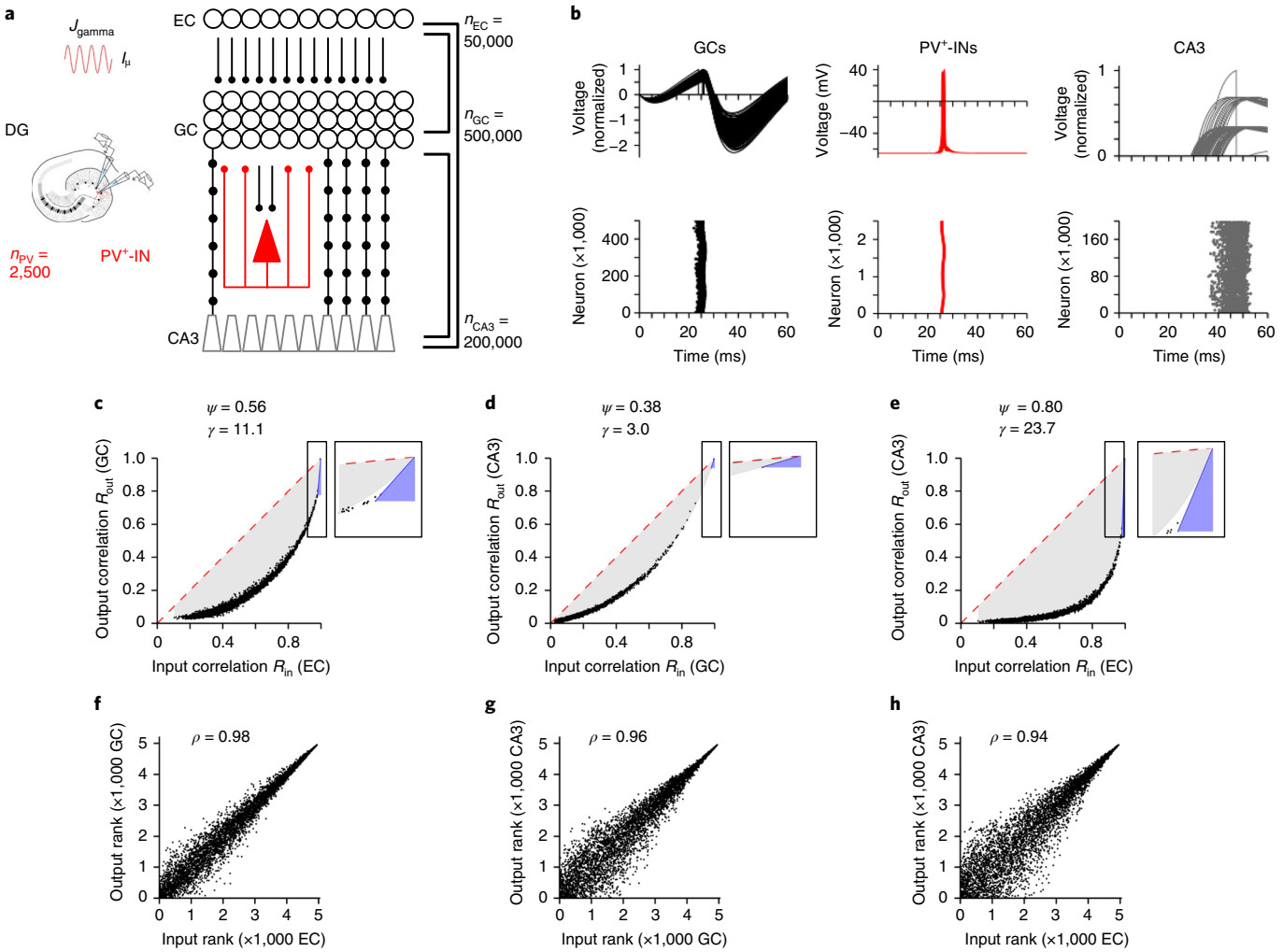

Fig. 1 | Pattern separation in a biologically realistic full-scale network model. a, Structure of the biologically inspired full-scale model based on experimental data on synaptic connectivity, and biophysical properties of cells and synapses. GCs and CA3 neurons were implemented as leaky integrate-and-fire (LIF) neurons. PV+-INs were represented as single-compartment conductance-based models endowed with modified Hodgkin–Huxley-type conductances[67] to convey maximal realism to the pattern separation mechanism. GCs were activated by a tonic excitatory drive (I_μ), and external inhibitory conductance was simulated to mimic gamma oscillations (J_{gamma}). Cell numbers (right) were chosen to represent the hippocampus of one hemisphere in rodents[13]. **b**, Activity in the pattern separation network model. Top: membrane potential in GCs (left), PV+-INs (center) and CA3 pyramidal neurons (right). Traces from every 10th IN (250 traces total) and every 1,000th GC or CA3 pyramidal cell (500 and 250 traces total, respectively) were superimposed. The membrane potential is unitless for GCs and CA3 pyramidal cells, as cells were simulated as LIF neurons. Bottom: raster plots of action potential generation in GCs (left), PV+-INs (center) and CA3 pyramidal neurons (right). Each point indicates an action potential; $t = 0$ corresponds to onset of inhibitory conductance representing a gamma oscillation cycle in the network[19]. **c**–**e**, Input–output correlation (R_{out}–R_{in}) graphs at different levels of the network (standard parameter settings). Data points represent pairwise correlation coefficients between R_{in} and R_{out}. Input–output correlation at the first layer, measured between EC neurons and GCs (**c**), at the second layer, measured between GCs and CA3 neurons (**d**) and across the entire network, measured between EC and CA3 neurons (**e**), are shown. The red dashed lines are identity lines, whereas the gray shaded areas represent the area between the data points and identity lines (used for computation of the integral-based pattern separation index, ψ). Blue lines and light blue shaded areas are tangent lines at $R_{in} = 1$ and corresponding slope triangles of a polynomial function fit to the data points, respectively (used for computation of slope-based pattern separation index, γ). Insets show a horizontally expanded view of the tangents and slope triangles used to compute γ. **f**–**h**, Preservation of rank order similarity between patterns at input and output; ρ was computed as the correlation coefficient of ranked R_{out} versus ranked R_{in} data. Rank analyses at the first layer, measured between EC and DG (**f**), at second layer, measured between DG and CA3 (**g**) and across the entire network, measured between EC and CA3 (**h**), are shown.

increased it (Fig. 3f, top). Similarly, increasing EC activity consistently decreased ψ (Fig. 3f, bottom). Changing the EC–GC connection probability had more complex effects, with the lowest values of ψ for intermediate connectivity, and highest values at both the low- and high-connectivity limit (Fig. 3g, top). Finally, increasing EC–GC connection width consistently decreased ψ (Fig. 3g, bottom); thus, the excitatory EC–GC connectivity only moderately influenced pattern separation. These results indicate that divergent connectivity was not strictly required for pattern separation, neither in a simplified model, nor in a biologically realistic full-scale network.

Requirement for local connectivity and fast PV+-IN signaling. Classical models suggest that global PN–IN connectivity supported pattern separation more effectively than local connectivity[9]; however, our results indicate that a model based on local connectivity

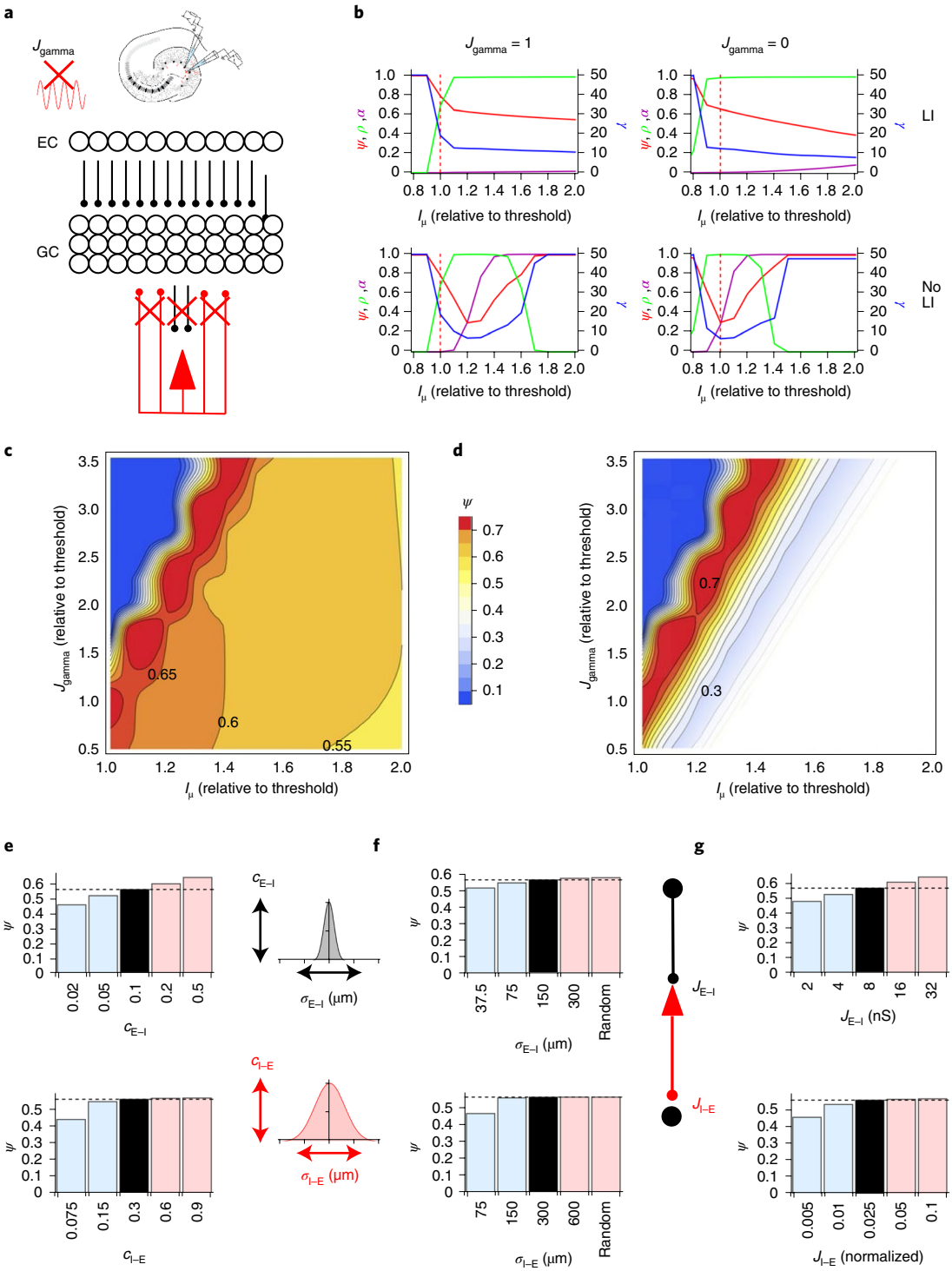

Fig. 2 | Dependence of pattern separation on gamma rhythm and lateral inhibition. a, Analysis of effects of inhibition on pattern separation in a biologically inspired full-scale model of the DG. Lateral inhibition was mediated by PV$^+$-INs included in the models. Gamma-modulated inhibition was included as synchronized external inhibitory conductance. **b**, Plots of ψ, γ, ρ and the average activity α against excitatory drive in GCs (I_{μ}). Top left: default model, with both gamma inhibition and lateral inhibition (LI) intact (J_{gamma} = 1 relative to threshold, J_{E-I} = 8 nS, J_{I-E} = 0.025, relative to threshold). Top right: gamma inhibition deleted (J_{gamma} = 0). Bottom left: lateral inhibition removed (J_{E-I} = 0, J_{I-E} = 0). Bottom right: both gamma inhibition and lateral inhibition cancelled from the default model (J_{gamma} = 0, J_{E-I} = 0, J_{I-E} = 0). **c**, Contour plot of ψ against the mean excitatory drive (I_{μ}, abscissa) and amplitude of gamma inhibition (J_{gamma}, ordinate). Contour lines indicate ψ. **d**, Similar contour plot as shown in **c**, but after removal of lateral inhibition. Analysis of pattern separation was restricted to the region of the I_{μ}–J_{gamma} parameter space in which $\alpha < 0.5$ (otherwise white). **e**–**g**, Interfering with lateral inhibition in different ways similarly affects pattern separation. Top: ψ for different values of peak connection probability of excitatory E–I connectivity (**e**), width of excitatory E–I connectivity (**f**) and synaptic strength of excitatory E–I synapses (**g**). Bottom: similar analysis, but for inhibitory I–E connectivity. Increasing c_{I-E}, σ_{E-I} or σ_{I-E} and J_{I-E} increased pattern separation efficacy only minimally, whereas increasing c_{E-I} and J_{E-I} led to much larger improvement; c_{I-E}, σ_{E-I} or σ_{I-E} and J_{I-E} thus appear to be near the optimum that provides maximal pattern separation, whereas c_{E-I} and J_{E-I} are below the optimum.

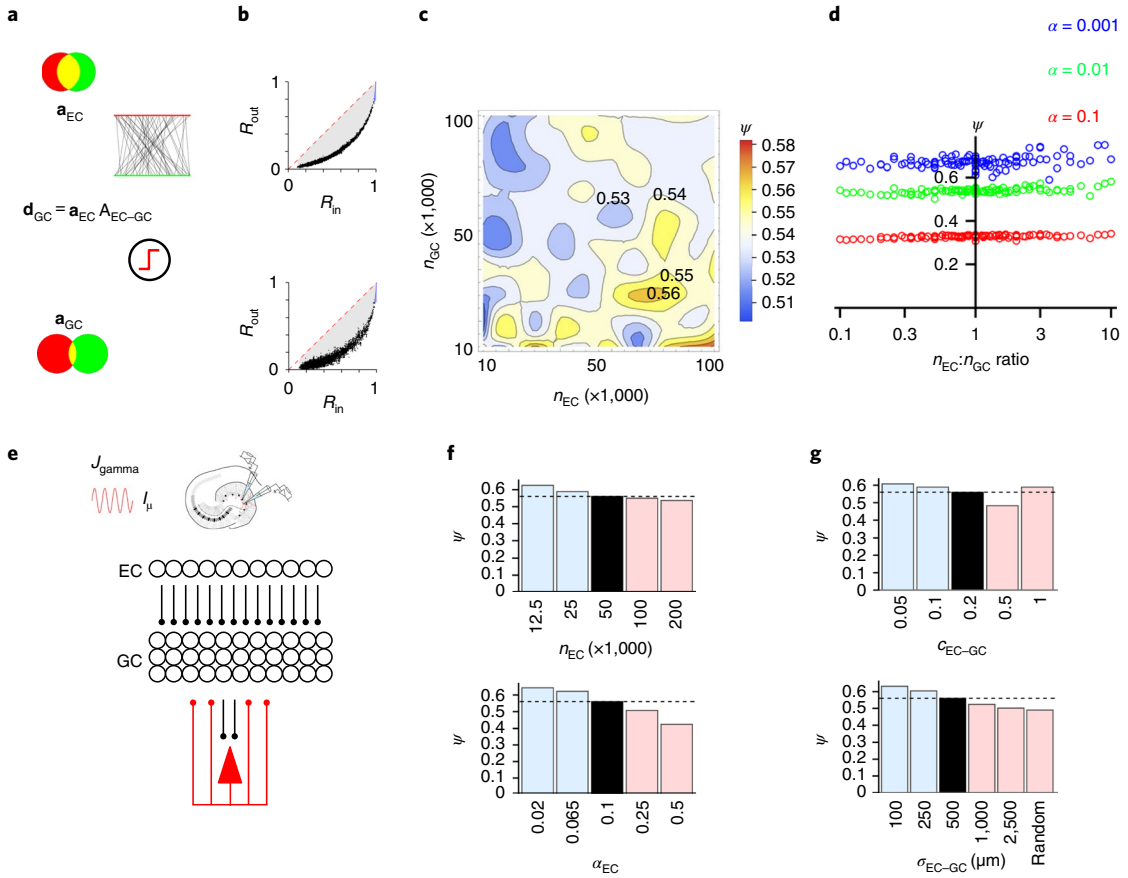

Fig. 3 | Moderate dependence of pattern separation on divergent excitatory connectivity between EC neurons and GCs. a, Analysis of divergence and convergence in a simplified connectivity-thresholding network. Binary activity vectors of the presynaptic layer were multiplied by a connectivity matrix, resulting in drive vectors in the postsynaptic layer. Drive vectors were then converted into binary vectors by thresholding. The threshold was set to obtain a defined α. **b**, R_{out} versus R_{in} for finite neuronal populations with different convergence–divergence ratios. Top: n_{EC}:n_{GC} = 10,000:100,000. Bottom: n_{EC}:n_{GC} = 100,000:10,000. **c**, Contour plot of ψ against the number of presynaptic neurons (n_{EC}, abscissa) and the number of postsynaptic neurons (n_{GC}, ordinate). In all simulations, α was set to 0.01. **d**, Plot of ψ against presynaptic–postsynaptic divergence ratio for different activity levels (red, α = 0.1; green, α = 0.01; blue, α = 0.001). **e**, Analysis of divergence and convergence in a full-scale biologically inspired model of the EC–DG circuit. **f**, Effects of changes in number of ECs (top) and activity level in EC neurons (bottom). **g**, Effects of maximal connection probability (top) and width of EC–GC connectivity (bottom).

rules[22] is a highly efficient pattern separator. We explored the effects of local E–I and I–E connectivity in the network model to resolve this apparent contradiction (Fig. 4a–c). To address the effects of locality in isolation, we maintained the total connectivity (that is the area under the connection probability–distance curve) through compensatory changes in maximal connection probability. Increasing the width of connectivity for either excitatory E–I or inhibitory I–E synaptic connections reduced ψ; particularly large changes were observed when local connectivity was replaced by global random connectivity (Fig. 4b). Local PN–IN connectivity thus supported pattern separation more effectively than global connectivity.

We next examined the effects of changes in the width of excitatory E–I and inhibitory I–E connectivity (Fig. 4c). As before, the total connectivity was maintained through compensatory changes in maximal connection probability. Contour plot analysis corroborated that local connectivity supported pattern separation more effectively than broad connectivity; however, the effects of changes in the width of excitatory E–I and inhibitory I–E connectivity were asymmetric. If focal E–I and I–E connectivity were equally important, ψ contour lines should have a slope of −1, yet the contour lines were much steeper (Fig. 4c). Hence, local excitatory E–I connectivity (plotted on the abscissa) was more important for pattern separation than local inhibitory I–E connectivity (plotted on the ordinate). The biological connectivity scheme, in which excitatory E–I is narrower than inhibitory I–E connectivity[22], is therefore highly suitable for pattern separation.

Why does local connectivity better support pattern separation than global connectivity? Effects of local connectivity might be a consequence of changes in average latency, which are shorter in a locally connected network than in an equivalent random network (Fig. 4d). To test this hypothesis, we first examined the effects of changes in axonal propagation velocity (v_{AP}). As predicted, decreases in both $v_{AP,E-I}$ and $v_{AP,I-E}$ negatively affected pattern separation (Supplementary Fig. 9a). Next, we changed the connectivity width while maintaining the average kinetic properties of disynaptic inhibition through compensatory changes of $v_{AP,E-I}$ and $v_{AP,I-E}$ (Supplementary Fig. 9b). Changes in propagation velocity almost completely compensated the effects of changes in connectivity. Local connectivity therefore improved pattern separation through facilitation of rapid signaling.

If local connectivity enhanced pattern separation by increasing the average speed of lateral inhibition, other fast signaling processes in INs may also contribute[21,46–48]. We systematically varied the corresponding model parameters to test this hypothesis (Fig. 4e,f). Increasing the synaptic delay at both excitatory GC–PV$^+$-IN synapses and inhibitory PV$^+$-IN–GC synapses impaired pattern

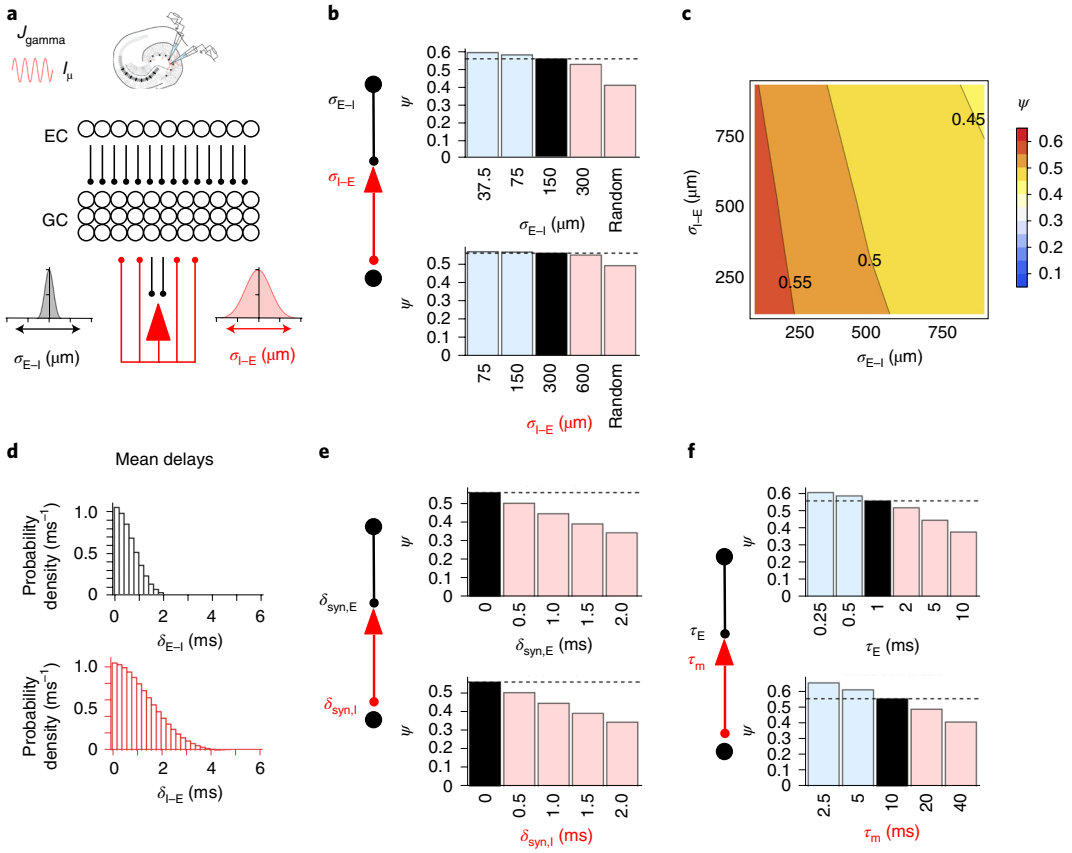

Fig. 4 | Requirement for local PN–IN interconnectivity and fast IN signaling. a, Analysis of lateral inhibition mechanisms in a biologically inspired full-scale model of the GC–PV$^+$-IN circuit. To determine the effects of local connectivity, the width of excitatory GC–PV$^+$-IN connectivity (σ_{E-I}) and inhibitory PV$^+$-IN–GC connectivity (σ_{I-E}) was varied. **b**, Effects of local connectivity on pattern separation. Summary bar graph of ψ for different values of excitatory σ_{E-I} (top) or inhibitory σ_{I-E} (bottom) connectivity in the network. The right bar in each bar graph (Random) represents uniform random connectivity. Peak connectivity (and, if required, synaptic strength) was compensated to maintain the total synaptic efficacy (different from Fig. 2f). **c**, Contour plot of ψ against width of excitatory E–I connectivity (σ_{E-I}) and inhibitory I–E connectivity (σ_{I-E}). Peak connectivity (and, if required, synaptic strength) was compensated to maintain the total synaptic efficacy. Asymmetry in spatial connectivity rules enhances pattern separation, consistent with experimental observation of narrower excitatory E–I connectivity and broader inhibitory I–E connectivity[22]. **d**, Distribution of axonal delay values in the network with standard parameters for excitatory E–I (top) and inhibitory I–E synapses (bottom). **e**, Summary bar graph of ψ for impairment of fast IN signaling by changes in synaptic delays at excitatory (top) and inhibitory (bottom) synapses. Note that the effects of synaptic delay are more powerful than the effects of propagation velocity (Supplementary Fig. 9a), highlighting the importance of synaptic properties, for example, the Ca^{2+} channel–release sensor coupling distance[61]. **f**, Summary bar graph of ψ for impairment of fast IN signaling by changes in the decay time constant of excitatory postsynaptic conductance $\tau_{decay,E}$ (top) and the membrane time constant of the interneuron τ_m (bottom). Interfering with fast signaling at multiple levels of the lateral inhibition pathway consistently impairs pattern separation.

separation (Fig. 4e). Notably, the effect was stronger than that of action potential propagation velocity (Supplementary Fig. 9a). Similarly, prolonging the time constants of the synaptic currents at excitatory GC–PV$^+$-IN synapses reduced pattern separation efficacy (Fig. 4f, top). Finally, slowing the membrane time constant of the PV$^+$-INs inhibited pattern separation (Fig. 4f, bottom). Thus, the fast signaling properties of PV$^+$-INs contributed to the efficacy of pattern separation process.

Contribution of mossy fiber synapses to pattern separation. In our standard model, the mossy fiber synapse between GCs and CA3 pyramidal neurons provides a substantial contribution to pattern separation (Fig. 1c–e). In the model, we realistically implemented both connectivity and synaptic strength of mossy fiber synapses. The number of mossy fiber synapses per GC was taken at 15, consistent with past morphological data[11,22,38]. The strength of hippocampal mossy fiber synapses was assumed to be subthreshold (with a synaptic strength/threshold ratio of 0.34), in agreement with previous experimental data showing that mossy fiber synapses have subthreshold properties under control conditions[25,39,40,49].

How does sparse connectivity of hippocampal mossy fiber synapses contribute to pattern separation? Whereas dense connectivity may introduce correlations, sparse connectivity may avoid such correlations[26]. We varied the number of mossy fiber terminals per axon to test this hypothesis (Fig. 5a–d). To maintain the activity level of the network, the individual synaptic conductance values were appropriately scaled. Increasing the number of mossy fiber boutons per axon unexpectedly increased the amount of pattern separation in the second layer of the network; ψ, measured between DG and CA3, increased from 0.37 to 0.61 (Fig. 5c,d). Similarly, ψ measured across the entire network increased from 0.80 to 0.92. The sparse connectivity of the mossy fiber synapse therefore decreases, rather than increases, the magnitude of pattern separation (Fig. 5d).

A hallmark property of mossy fiber synapses is the unique extent of presynaptic plasticity, including facilitation, post-tetanic

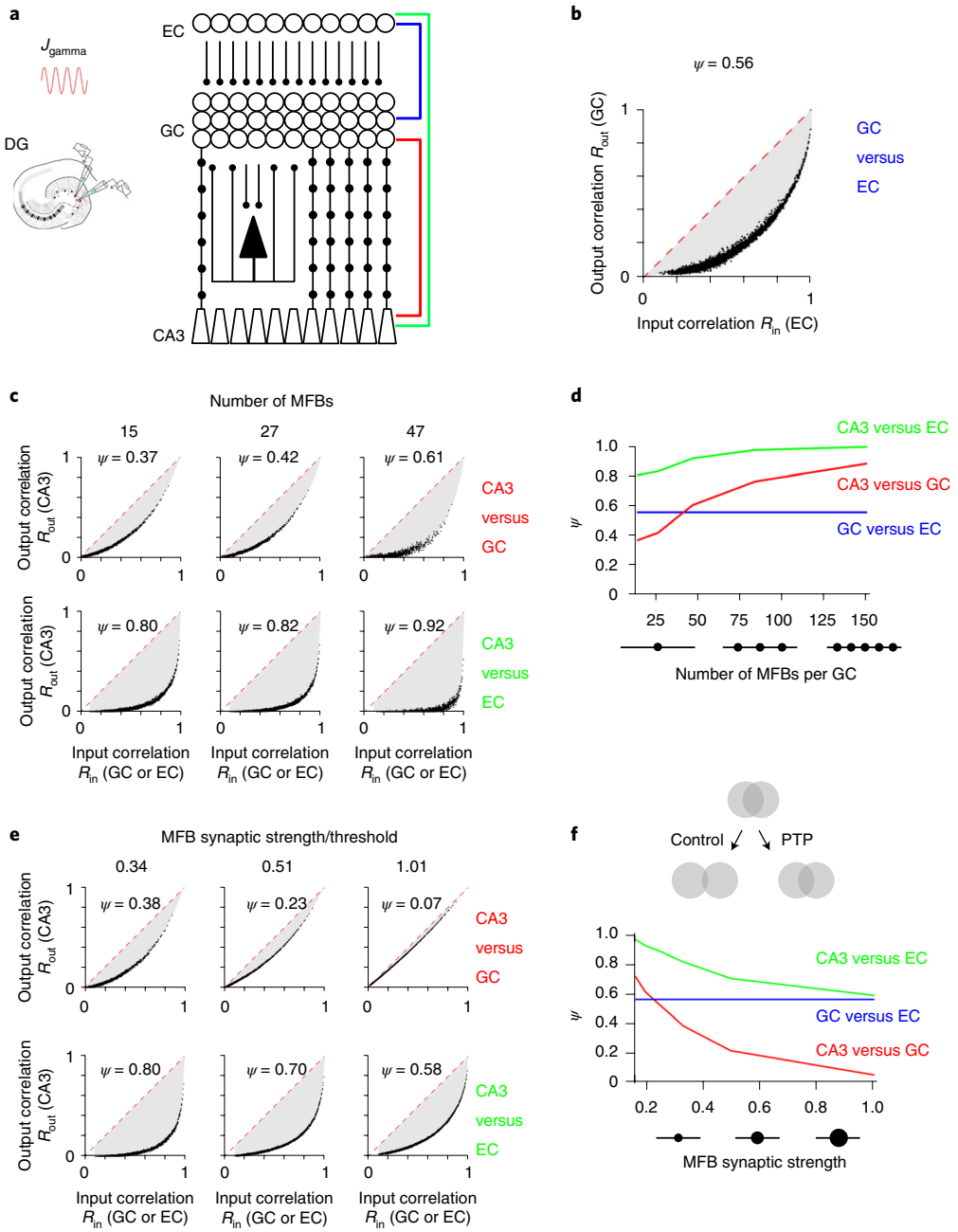

Fig. 5 | Contribution of hippocampal mossy fiber synapses to pattern separation. a, Analysis of effects of multilayer structure of the hippocampal network on pattern separation in a biologically inspired full-scale model of the EC–DG–CA3 circuit. To address the effects of mossy fiber output, the GC–PV$^+$-IN network was connected to a CA3 network via synapses with mossy fiber-like properties. **b**, R_{out}–R_{in} graph for the EC–DG component of the network. Same graph as shown in Fig. 1c. **c**, R_{out}–R_{in} graphs for the DG–CA3 component of the network (top) and the entire system (bottom) for different numbers of mossy fiber boutons per axon. **d**, ψ plotted against number of mossy fiber boutons per axon. Blue, isolated EC–DG component; red, isolated DG–CA3 mossy fiber component; green, total EC–DG–CA3 system. In both **c** and **d**, synaptic strength was compensated to maintain the total synaptic efficacy. **e**,**f**, Similar plots as in **c** and **d**, but for variation of synaptic strength of mossy fiber synapses relative to threshold. The inset is a schematic illustration of how presynaptic plasticity at mossy fiber synapses affects pattern separation. Left: situation before induction of synaptic plasticity (control). Right: situation after induction of presynaptic plasticity, for example, facilitation or PTP[25,40]. Two patterns are efficiently separated in the absence of PTP (left), but less so after PTP induction (right).

potentiation (PTP) and long-term potentiation[25,40,50]. To examine how these specific plasticity properties influence pattern separation, we systematically shifted synaptic strength in the range from the subdetonation into the detonation range (Fig. 5e,f). When synaptic strength relative to threshold was increased from 0.34 to 0.51 and 1.01, ψ measured between DG and CA3 progressively reduced (ψ = 0.38, 0.23 and 0.07, respectively; Fig. 5e, top; Fig. 5f). Similarly, ψ measured across the entire network became smaller (ψ = 0.80, 0.70 and 0.58, respectively; Fig. 5e, bottom; Fig. 5f). Presynaptic plasticity at hippocampal mossy fiber synapses thus shifted the network from strong to weak pattern separation, that is, in the direction of pattern completion (Fig. 5f).

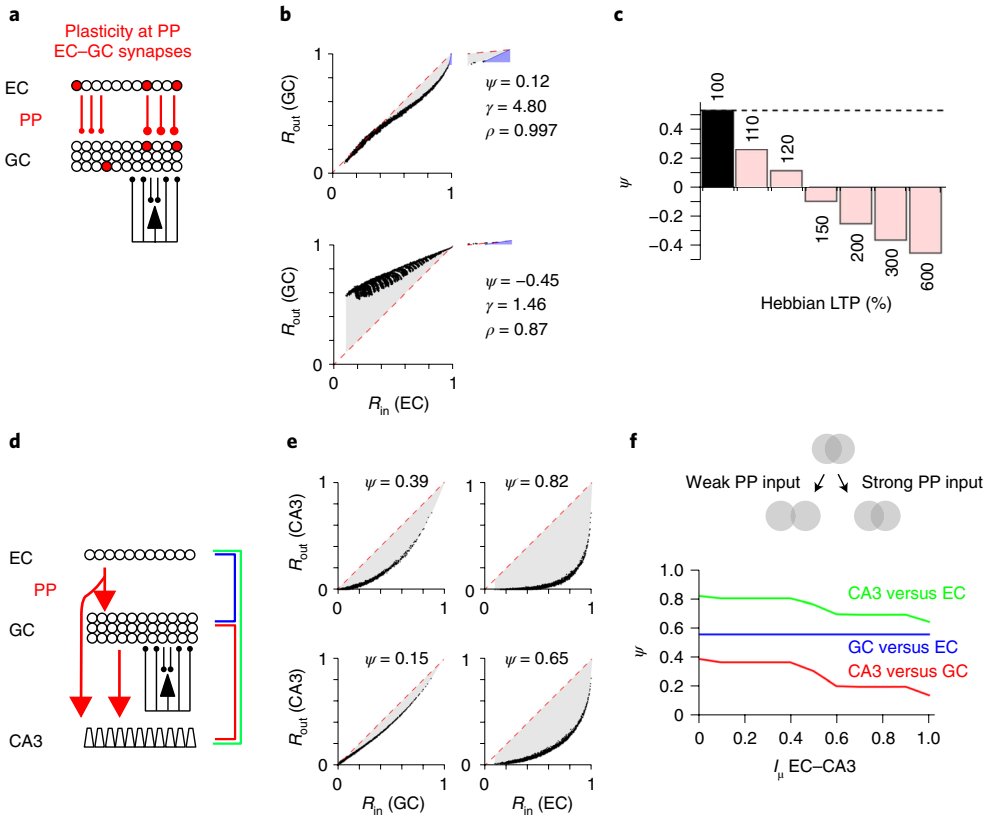

Fig. 6 | Contribution of PP input to pattern computations. a–c, Hebbian plasticity at PP EC–GC synapses switches the network from pattern separation to pattern completion. **a**, Schematic illustration of the model that incorporates Hebbian plasticity at PP EC–GC synapses. Synaptic plasticity was implemented according to a Hebbian rule and a sigmoidal relation between potentiation and the number of coincident action potentials (Methods). **b**, R_{out}–R_{in} curve with 120% (top) and 600% (bottom) plasticity factor at PP EC–GC synapses. **c**, Summary bar graph of ψ for various Hebbian synaptic plasticity potentiation factors; ψ in control conditions (100%; black) was slightly lower than in Fig. 1, as R_{in} was computed from binary EC patterns rather than analog drive patterns. **d–f**, Direct PP input to CA3 pyramidal neurons (EC–CA3 input) regulates the balance between pattern separation and pattern completion. **d**, Schematic illustration of the model incorporating a direct PP connection from the EC to the CA3 region. **e**, R_{out}–R_{in} graphs for the DG–CA3 component of the network (left) and the entire EC–DG–CA3 network (right) for I_{μ} EC–CA3 = 0 (top) and I_{μ} EC–CA3 = 1 (bottom). **f**, ψ plotted against I_{μ} EC–CA3. Plateaus in the relation correspond to different integer numbers of mossy fiber terminals required for postsynaptic spiking.

Contribution of PP synapses to pattern completion. The role of Hebbian plasticity at PP EC–GC synapses in pattern separation has been unclear[30,31]. To test the effects of Hebbian synaptic plasticity at PP synapses on pattern computations in the network, we initially simulated the responses of the network to 100 EC patterns with the default parameter set in a control run, potentiated the PP EC–GC synapses according to a simple Hebbian synaptic plasticity rule and subsequently simulated the responses of the network to 100 EC patterns with the potentiated synapses in a test run (Fig. 6a–c). Whereas the network demonstrated robust pattern separation under control conditions, potentiation according to a Hebbian plasticity rule reduced both ψ and γ, switching the network from a pattern separation into a pattern completion mode (Fig. 6a–c).

PP inputs not only innervate GCs[27], but also CA3 pyramidal neurons via PP EC–CA3 synapses[32]. Do these synapses also regulate pattern separation in the EC–DG–CA3 network? To address this question, a tonic excitatory drive computed from the EC activity and the EC–GC connectivity was applied in parallel to GCs and CA3 pyramidal neurons after appropriate scaling to represent feed-forward excitation. Increasing the strength of the PP EC–CA3 synapses markedly reduced the degree of pattern separation (Fig. 6d–f). Taken together, our results indicate that mossy fiber GC–CA3 and PP EC–CA3 synapses synergistically regulate pattern computations, shifting the EC–DG–CA3 network from pattern separation in the direction of pattern completion.

Discussion

A fundamental question in neuroscience is how higher-order computations are implemented at the level of synapses, neurons and neuronal networks. Our full-size, realistic network model provides an answer to this question, at least for a specific network function (pattern separation) and a specific circuit (the EC–DG–CA3 circuit). This information may be useful to expand the deep learning capabilities of technical networks[51].

According to the Marr–Albus theory, divergence of excitatory connections plays a major role in pattern separation[4,9,10,52]. However, in the trisynaptic pathway, divergence at EC–GC synapses is followed by convergence at GC–CA3 pyramidal neuron synapses. How is pattern separation possible under these conditions? As the mossy fiber synapse is below the threshold of action potential initiation in postsynaptic CA3 cells[25], convergence followed by thresholding will establish a decorrelation mechanism[15,53]. Pattern separation in the mossy fiber system will accumulate with pattern separation generated in the DG, leading to increase of ψ across layers. Pattern separation is thus not strictly localized to the DG, but represents a distributed network computation that involves multiple regions of the trisynaptic circuit.

Thresholding is a well-established decorrelation mechanism[15,53,54]. Consistent with the idea that thresholding contributes to pattern separation in the DG, GCs show a uniquely negative resting membrane potential and a high relative voltage threshold[55]. Although our

results confirm that thresholding in the complete absence of inhibition can result in pattern separation, efficient pattern separation is only possible in a narrow region of the parameter space. Addition of lateral inhibition markedly expands the regime of efficient pattern separation (Fig. 2c,d). This is consistent with behavioral experiments showing that both genetic deletion of $GABA_A$ receptors in GCs and pharmacogenetic inhibition of GABAergic INs in the DG affect pattern separation[56,57].

Both experimental and theoretical evidence suggests that network oscillations, particularly in the gamma frequency range, may play a role in pattern separation[19,58]. We have incorporated gamma activity as a transient inhibitory conductance at the simulation onset and found that this conductance enhanced pattern separation. It is possible that gamma oscillations and pattern separation are different reflections of the same phenomenon, for example disynaptic inhibition. Alternatively, gamma oscillations in the DG may be generated by mutual inhibition[37,59]. In this scenario, rhythmic gamma activity may assist pattern separation by structuring activity in time[58]. Mutual inhibition and recurrent inhibition thus may cooperate to provide an optimal framework for pattern separation.

Several theories assume that global lateral inhibition plays a key role in pattern separation[4,9]. Intuitively, global inhibition could implement a winner-takes-all or a k-winners-take-all mechanism[14,18,19,43,44]. In the DG, lateral inhibition is abundant, but follows local distance-dependent connectivity rules[22]. How can a local lateral inhibition mechanism contribute to pattern separation? Our model unexpectedly reveals that local connectivity supports pattern separation even more effectively than global connectivity. The beneficial effects of local connectivity are almost completely compensated by reducing the signaling speed; thus, local connectivity enhances pattern separation through a gain in the speed of lateral inhibition.

Fast signaling is a hallmark of function of GABAergic INs, particularly fast spiking, PV^+ subtypes[46]. Fast signaling properties are expressed at multiple levels, including excitatory synaptic input[21,22], input–output transformation[47], axonal action potential propagation[60] and inhibitory synaptic output[48]; however, the impact of these specific signaling properties on higher-order computations in neuronal networks is unclear. Here we show that several fast signaling properties of GABAergic INs facilitate pattern separation. Short synaptic delays are particularly critical for pattern separation, suggesting that tight coupling between presynaptic Ca^{2+} channels and release sensors might be important[61]. Furthermore, the decay time constant of the excitatory synaptic conductance at PN–IN synapses affects pattern separation, implying that the subunit composition of postsynaptic α-amino-3-hydroxy-5-methyl-4-isoxazolepropionic acid-type glutamate receptors in INs is relevant; thus, both pre- and postsynaptic molecular and subcellular specializations of PN–IN synapses contribute to the pattern separation at the network level.

Our model provides clues how the mossy fiber synapse contributes to pattern separation[23,62]. Pattern separation is not only relayed to the CA3 region, but rather conditionally amplified by the mossy fiber–CA3 synaptic connections (Fig. 1d,e; Fig. 5). The degree of amplification is determined by the properties of the synapse. Subdetonation properties will increase pattern separation, whereas detonation will reduce it. Previous work showed that the efficacy of mossy fiber synapses can be regulated by presynaptic plasticity mechanisms, which increase synaptic strength by almost one order of magnitude[25,40]. This suggests that mossy fiber plasticity might tune the balance between pattern separation and pattern completion. As a corollary, bursts or superbursts in GCs may shift the network from strong to weaker pattern separation, that is in the direction of pattern completion[33,40].

Hebbian synaptic plasticity is a hallmark property of PP EC–CA3 synapses[28,29]. Our results suggest that PP plasticity switches the network from pattern separation to completion. This may seem counter-intuitive, as a Hebbian rule based on presynaptic (original) patterns and postsynaptic (decorrelated) patterns might represent a feedback signal amplifying decorrelation[15]; however, in our simulations we applied 100 patterns with varying degree of overlap. As plasticity induction requires multiple pre-post pairings, this preferentially strengthens the overlapping synapses, leading to an increase of correlation; thus, whereas lateral inhibition consistently mediates pattern separation, PP plasticity may, at least with the chosen induction rules, promote pattern completion[31]. As a corollary, inhibition-based pattern separation could dominate at early time points (that is, with novel patterns), whereas plasticity-based pattern completion may prevail later (that is, with familiar patterns).

Perforant path inputs not only innervate GCs, but also CA3 pyramidal neurons via PP EC–CA3 synapses[32]. In a simplified model, the mossy fiber pathway conveys decorrelated patterns, whereas the PP input relays the original patterns to postsynaptic CA3 cells[23]. The effects of the excitatory drive from the EC–CA3 synapses are consistent with this idea. However, our analysis further suggests that increasing the EC–CA3 drive reduces the contribution of the mossy fiber synapses to the total pattern separation process (Fig. 6f). Intuitively, the EC–CA3 drive regulates the detonator properties of the mossy fiber–CA3 synapses by changing the effective firing threshold. Complex interactions between excitatory and inhibitory synapses therefore regulate the balance between pattern separation and completion.

Our biologically inspired network model is an efficient pattern separator; however, the network also may be able to perform other related higher-order computations. The pattern separation reliability ρ is close to 1, implying that rank similarity in the patterns is accurately preserved during information processing. Furthermore, the pattern separation gain γ is highest (>10) for very similar patterns, demonstrating that small differences at the input level are amplified into large differences at the output level. These functional properties will be suitable to run similarity searches (termed locality-sensitive hashing in computer science[35]) or to perform similarity-based clustering of contextual input information[63]. The EC–DG–CA3 network may therefore be computationally more powerful than previously thought.

Finally, our network model may help to develop new algorithms and computational architectures of technical deep learning networks[51]. Deep learning algorithms successfully incorporated the multilayer structure of biological networks, the hippocampal network being the prototype. Although such technical networks are remarkably powerful, they lack the robustness, energy efficiency and memory capability of biological networks. Incorporation of fast lateral inhibition and presynaptic short-term memory may increase the efficacy of such systems.

Full-size implementation is a strength of the present study; however, limitations were unavoidable. These include use of simplified cellular units (that is, integrate-and-fire neurons for GCs, single-compartment neurons for INs), lack of less abundant cell types (such as somatostatin$^+$ or vasointestinal peptide$^+$ GABAergic interneurons, mossy cells, and newborn GCs)[64,65], and simplified connectivity rules (for example, for PP EC–GC connections where experimental connectivity data are currently unavailable). Increase in computational power of modeling hardware may allow us to address these limitations in the future.

Methods

Topology of a full-size DG network model. The pattern separation network model consists of three layers: the first representing the EC, with 50,000 ECs; the second representing the DG, with 500,000 GCs and 2,500 PV^+-INs; and the third representing the CA3 region, with 200,000 pyramidal cells. The first and second layers were connected by EC–GC synapses, representing the PP input to the DG. A winner-takes-all mechanism mediated by lateral inhibition was implemented by connecting GCs and INs by excitatory E–I synapses in one direction, and by inhibitory I–E synapses in the other direction. The second and third layers were

connected by GC–CA3 pyramidal neuron synapses, representing hippocampal mossy fiber synapses.

Unlike many network models, our model was implemented in full size (Supplementary Table 1). The number of GCs was chosen to represent the DG of one hemisphere of adult laboratory mice[13]. Full-scale implementation was necessary: (1) to increase the realism of the simulations; (2) to be able to implement measured macroscopic connectivity rules without scaling[66]; and (3) to simulate sparse coding regimes, which were unstable in smaller networks. The model was designed to incorporate the connectivity rules of PV$^+$-INs and GCs in the DG (Supplementary Table 1)[22]. Other types of INs were not implemented in the default model, due to their lower connectivity[22] and their slower signaling speed[46]. In total, the conclusions of the present paper were based on 784 full-scale simulations.

Implementation of inhibitory INs. INs were implemented as single-compartment, conductance-based neurons endowed with modified Hodgkin–Huxley-type conductances[67] to capture the electrical properties of PV$^+$-INs. Membrane potential was simulated by solving the equation:

$$\frac{dV}{dt} = \frac{1}{C_m}\left(I_{drive} - I_{Na} - I_K - I_L\right), \quad (1)$$

where V is membrane potential; t is time; C_m is the capacitance of the membrane; I_{drive} is driving current; and I_{Na}, I_K and I_L represent sodium, potassium and leakage current, respectively. I_{Na} was modeled as

$$I_{Na} = \overline{g_{Na}}\, m^3 h (V - V_{Na}), \quad (2)$$

where $\overline{g_{Na}}$ is the maximal sodium conductance, m is the activation parameter, h is the inactivation parameter and V_{Na} represents the sodium ion equilibrium potential.

Similarly, I_K was modeled according to the equation

$$I_K = \overline{g_K}\, n^4 (V - V_K), \quad (3)$$

where $\overline{g_K}$ is the maximal potassium conductance, n is the activation parameter and V_K represents the potassium ion equilibrium potential.

Finally, I_L was given as

$$I_L = g_L (V - V_L), \quad (4)$$

where g_L is leakage conductance and V_L is corresponding reversal potential.

State parameters m, h and n were computed according to the differential equation

$$\frac{dm}{dt} = \alpha_m (1 - m) + \beta_m m \quad (5)$$

and equivalent equations for h and n.

α_m, α_h, α_n values and β_m, β_h, β_n values were calculated according to the equations $\alpha_m = 0.1\,ms^{-1} \times -(V+35\,mV)/\{\exp[-(V+35\,mV)/10\,mV] - 1\}$, $\beta_m = 4\,ms^{-1} \times \exp[-(V+60\,mV)/18\,mV]$, $\alpha_h = 0.35\,ms^{-1} \times \exp[-(V+58\,mV)/20\,mV]$, $\beta_h = 5\,ms^{-1}/\{\exp[-(V+28\,mV)/10\,mV] + 1\}$, $\alpha_n = 0.05\,ms^{-1} \times -(V+34\,mV)/\{\exp[-(V+34\,mV)/10\,mV] - 1\}$ and $\beta_n = 0.625\,ms^{-1} \times \exp[-(V+44\,mV)/80\,mV]$[67]. Single neurons were assumed to be cylinders with diameter and length of 70 µm, giving a surface area of 15,394 µm^2 and an input resistance of 65 MΩ (ref. [47]). Neurons showed a rheobase of 39 pA and a fast-spiking, type-I action potential phenotype[68], as characteristic for PV$^+$-INs[46]. Maximal conductance values were set as as $\overline{g_{Na}} = 35\,mS\,cm^{-2}$, $\overline{g_K} = 9\,mS\,cm^{-2}$ and $g_L = 0.1\,mS\,cm^{-2}$; V_{Na} V_K and V_L were assumed as 55 mV, −90 mV and −65 mV, respectively[67].

Implementation of GCs. GCs were implemented as spiking neurons with LIF firing properties, accelerating all computations by approximately one order of magnitude. To enable the integration of excitatory and inhibitory synaptic events with different kinetics, the standard LIF model was extended as follows[69]:

The time course of synaptic excitation was described by the differential equation

$$\frac{de}{dt} = -k_e\, e, \quad (6)$$

where k_e is the synaptic excitation rate constant, that is, the inverse of the time constant.

Likewise, the time course of synaptic inhibition was described by the differential equation

$$\frac{di}{dt} = -k_i\, i, \quad (7)$$

where k_i is the synaptic inhibition rate constant.

Finally, the firing of the neuron was controlled by a membrane state variable v; when v reaches 1, the cell fires, which resets the membrane by returning v to 0. The time course of v was determined by the differential equation

$$\frac{dv}{dt} = -k_m v + a_e e + a_i i + i_{drive}, \quad (8)$$

where k_m is inverse of the membrane time constant, a_e and a_i are amplitudes of synaptic events, and i_{drive} represents the excitatory drive any given neuron receives[69]. The excitation, inhibition and membrane time constants were set to 3, 10 and 15 ms, respectively (Supplementary Table 1)[22,48,70]. The refractory period was assumed to be 5 ms.

Implementation of synaptic interconnectivity. Synapses between neurons were placed with distance-dependent probability. Normalized distance was cyclically measured as

$$x = 0.5 - \mathrm{abs}\left\{\mathrm{abs}\left[(i/i_{max} - j/j_{max})\right] - 0.5\right\}, \quad (9)$$

where i and j are indices of pre- and postsynaptic neurons, respectively; i_{max} and j_{max} are the corresponding maximum index values; and abs(r) is the absolute value of a real number, r. Connection probability was then computed with a Gaussian function as

$$p(x) = ce^{-\frac{x^2}{2\sigma^2}}, \quad (10)$$

where c is the maximal connection probability (c_{E-I}, c_{I-E}, c_{I-I} and c_{gap}) and σ is the standard deviation representing the width of the distribution (σ_{E-I}, σ_{I-E}, σ_{I-I} and σ_{gap}; Supplementary Table 1).

The connection probability between ECs and GCs was computed from a Gaussian function with peak connection probability of 0.2 and a standard deviation of 500 µm, to represent the divergent connectivity from the EC to the DG[27,32,45]. Binary activity patterns in upstream ECs were converted into patterns of excitatory drive of GCs. Although this drive was primarily intended to represent input from EC neurons, it may include contributions from other types of excitatory neurons[64].

Excitatory GC–IN synapses, inhibitory IN–GC synapses, and inhibitory IN–IN synapses were incorporated by random placement of NetCon objects in NEURON[69]; gap junctions between PV$^+$-INs were implemented by random placement of pairs of point processes. For excitatory GC–IN synapses and inhibitory IN–IN synapses, synaptic events were simulated using the Exp2Syn class of NEURON. For excitatory GC–IN synapses, we assumed $\tau_{rise,E} = 0.1$ ms, $\tau_{decay,E} = 1$ ms and a peak conductance of 8 nS (Supplementary Table 1)[21,22]. For inhibitory IN–IN synapses, we chose $\tau_{rise,I} = 0.1$ ms, $\tau_{decay,I} = 2.5$ ms and a peak conductance of 16 nS (Supplementary Table 1)[22,37,59]. For inhibitory IN–GC synapses, the synaptic weight of 0.025 was chosen (which is unitless as GCs were modelled as LIF neurons). For all chemical synapses, the synaptic latency was between 0 and 25 ms, according to distance between pre- and postsynaptic neuron. The gap junction resistance was assumed to be 300 MΩ, approximately five times the input resistance of a single cell (Supplementary Table 1)[22,37,59]. Synaptic reversal potentials were 0 mV for excitation and −65 mV for inhibition. The maximal length of the hippocampal network was assumed to be 5 mm, consistent with anatomical descriptions in mice[71].

Detailed implementation and simulations. Simulations of network activity were performed using NEURON v.7.6.2, v.7.7.2 or v.7.8.2 (ref. [69]) in combination with Mathematica v.11.3.0.0 or v.12.2.0.0 (Wolfram Research). Simulations were tested on a Lenovo T470p PC running under Windows 10. Final full-size simulations were run on the IST computer cluster under Debian GNU/Linux v.9 or v.10 (https://www.debian.org/), the scheduling system Slurm 16.05, and the environment module system Lmod 7.7.

Simulations were performed in four steps (Supplementary Fig. 1). First, we computed random binary activity patterns in ECs. To generate input patterns with defined correlations over a wide range, 100 uncorrelated random vectors $\mathbf{a}_i$ of size n_{EC} were computed, where individual elements are pseudorandom real numbers in range of 0 to 1 and n_{EC} is the number of ECs. Uncorrelated vectors were transformed into correlated vectors as $r \times \mathbf{a}_1 + (1-r) \times \mathbf{a}_i$, where $\mathbf{a}_1$ is the first random vector and r is a correlation factor; r was varied between 0.1 and 1. Finally, a threshold function $f(x) = \mathrm{H}(x - \theta)$ was applied to the vectors, where H is the Heaviside function and θ is the threshold that determines the activity level in the pattern. Empirically, 100 input patterns were sufficient to continuously cover the chosen range of input correlations. Unless stated differently, the average activity in EC neurons (α_{EC}), that is the proportion of spiking cells, was assumed to be 0.1.

Second, the patterns in the upstream neurons were converted into patterns of excitatory drive in GCs, by multiplying the activity vectors with the previously computed connectivity matrix between EC neurons and GCs. Unless otherwise indicated, the mean tonic current value was set to 1.8 times the threshold value of the GCs (that is $I_\mu = 1.8$; unitless, as GCs were implemented as LIF units; Supplementary Table 1).

Third, we computed the activity of the network for all 100 patterns. Simulations were run with 5 µs fixed time step over a total duration of 50 or 60 ms. At the beginning of each simulation, random number generators were initialized with defined seeds to ensure reproducibility. At $t=0$, an inhibitory synaptic event of weight 1 (relative to threshold) was simulated in all GCs to mimic recovery from gamma-modulated inhibition[19]. Spikes were detected when membrane potential reached a value of 1 in the GCs and 0 mV in the INs. Subsequently, spike times were displayed in raster plot representations. Furthermore, 100 binary output vectors were computed, by setting the value to 1 if a cell generated ≥1 spikes in the simulation time interval, and to 0 otherwise.

Finally, Pearson's correlation coefficients were calculated for all pairs of patterns ($\binom{100}{2}$ = 4,950 points), at both input and output level in parallel as

$$R = \frac{\mathrm{Cov}(\mathbf{n}_1, \mathbf{n}_2)}{\sqrt{\mathrm{Var}(\mathbf{n}_1)\,\mathrm{Var}(\mathbf{n}_2)}}, \tag{11}$$

where Cov is covariance, Var is variance, and $\mathbf{n}_1$ and $\mathbf{n}_2$ are two given pattern vectors. Due to mean value subtraction and normalization, this correlation measure is per se independent of activity[53]. Next, output correlation coefficients (R_{out}) were plotted against input correlation coefficients (R_{in}). For models activated by Poisson trains of PP input (Supplementary Fig. 3) or implementing variation of synaptic amplitude (Supplementary Fig. 7), R_{out}–R_{in} curves were normalized to the average R_{out} values obtained for identical patterns ($R_{in}=1$), which were <1 due to the stochastic nature of the models. For models with heterogeneity of excitability (Supplementary Fig. 8), R_{out}–R_{in} curves were normalized to the average R_{out} values obtained for uncorrelated patterns ($R_{in}\to 0$), which were greater than zero as the cells with the highest excitability were consistently firing, whereas the cells with the lowest excitability were consistently silent. Pattern separation was quantitatively characterized by three parameters: (1) the efficacy of pattern separation (ψ) was quantified by an integral-based index, defined as the area between the identity line and the R_{out} versus R_{in} curve, normalized by the area under the identity line ($\frac{1}{2}$). Thus,

$$\psi = 2\int_{x=0}^{1} (x - f(x))\mathrm{d}x, \tag{12}$$

where $f(x)$ represents the input-output correlation function. In practice, data points were sorted by R_{in} values, and points with same R_{in} were averaged. $f(x)$ was determined as a 5th or 10th-order polynomial function $f(x)$ fit to the R_{out} versus R_{in} data points; $f(x)$ was constrained to pass through points (0|0) and (1|1). Based on the definition of equation (12), a ψ value close to 1 would correspond to an ideal pattern separator. By contrast, $\psi=0$ would represent pattern identity, whereas $\psi<0$ would indicate pattern completion. (2) The gain of pattern separation (γ) was quantified from the maximal slope of the R_{out} versus R_{in} curve. In practice, this value was determined from the first derivative of the polynomial function $f(x)$ fit to the R_{out} versus R_{in} data points as $\lim_{x\to 1}\left(\frac{df(x)}{dx}\right)$. A γ value ≫1 would correspond to an ideal pattern separator. By contrast, $\gamma=1$ would represent pattern identity, whereas $\gamma<1$ may indicate pattern completion. (3) The reliability of pattern separation (ρ) was quantified by the Pearson's correlation coefficient of the ranks of all R_{out} versus the ranks of the corresponding R_{in} data points. An ideal pattern separator will maintain the order of pairwise correlations: if a pair of patterns is more similar than another pair at the input level, it will be also more similar at the output level; thus, ρ will be close to 1 for an ideal pattern separator (refs. [34–36]).

To analyze the effects of convergence and divergence on pattern separation (Fig. 3a–d), activity was simulated in ECs, converted into drive patterns in GCs by multiplication with the EC–GC connectivity matrix, and finally converted into binary activity values in GCs by applying a threshold corresponding to the desired α. This simplified approach permitted systematic variation of model parameters (for example, cell numbers and connection probabilities) over a wide range. In the simulations, both n_{EC} and n_{GC} was varied between 10,000 and 100,000, yielding ratios ranging from 1:10 to 10:1. Unless specified differently, in these simplified simulations, α_{EC} was set to 0.1 and EC–GC connectivity was assumed to be random with an average connection probability ($c_{EC\text{–}GC}$) of 0.05

To address the effects of plasticity at PP synapses on pattern computations (Fig. 6a–c), we introduced an associative synaptic plasticity rule at EC–GC synapses. We first simulated the responses of the network to 100 EC patterns with the default parameter set in a control run. Coincident pre- and postsynaptic activity was cumulatively recorded for all synapses across all patterns. We next computed the extent of potentiation for each EC–GC synapse according to a sigmoidal function of the form

$$f(x) = f_{pot}/\left(1 + \exp\left[-\left(x - x_{half}\right)/k\right]\right), \tag{13}$$

where f_{pot} is the potentiation, x is the number of coincident action potentials, x_{half} is the number of action potentials leading to half-maximal potentiation, and k is a slope factor. As default values, $x_{half}=5$ and $k=5$ were used. Finally, we simulated the responses of the network to 100 EC patterns with the potentiated synapses in a test run (Fig. 6a–c).

Robustness of the pattern separation mechanism. Unless specified differently, standard parameter values (Supplementary Table 1) were used for all simulations. However, several additional simulations were performed to test the robustness of pattern separation against parameter variation. (1) To test the effects of conductance-based synapses against current-based synapses (Supplementary Fig. 2), GCs were simulated as single-compartment conductance-based neurons with passive properties. (2) To test the effects of temporal structure of the excitatory drive (Supplementary Fig. 3), the tonic current was replaced by Poisson trains of synaptic events. In these simulations, events were simulated by NetStim processes. (3) To generate spatially correlated patterns (Supplementary Fig. 4), random numbers were drawn from a multinormal distribution with exponential spatial correlation (length constant 15,000 cells) and thresholded to give a spatially correlated binary pattern with appropriate activity level. (4) To implement feedforward inhibition (Supplementary Fig. 5), the tonic excitatory drive computed from EC activity and EC–GC connectivity was applied in parallel to INs after appropriate scaling. (5) To replace PV$^+$-INs with cholecystokinin (CCK)$^+$-like IN subtypes (for example hilar INs with axons associated with the commissural / associational pathway; Supplementary Fig. 6a)[72–75], model parameters were changed to account for reduced connectivity, altered synaptic strength, and slower signaling according to the replacement rules $c_{E\text{-}I}=0.1\to 0.02$, $c_{I\text{-}E}=0.3\to 0.1$, $J_{E\text{-}I}=0.008\to 0.004$ nS, $J_{I\text{-}E}=0.025\to 0.05$, $\tau_{I\text{-}E}=10\to 20$ ms, and $\tau_m=10\to 20$ ms. Furthermore, to incorporate CCK$^+$-like IN subtypes in the network (Supplementary Fig. 6b), an increasing number of neurons with the following connectivity parameters were added to the model: $c_{CCK\text{–}CCK}=0.2$, $c_{PV\text{–}CCK}=0.6$, $c_{CCK\text{–}PV}=0.2$, $c_{E\text{–}CCK}=0.02$, $c_{CCK\text{–}E}=0.1$, $J_{E\text{–}CCK}=4$ nS, $J_{CCK\text{–}E}=0.05$, $J_{CCK\text{–}CCK}=16$ nS, $J_{PV\text{–}CCK}=16$ nS and $J_{CCK\text{–}PV}=16$ nS. (6) To incorporate PP inputs to CA3 pyramidal neurons (Fig. 6d–f)[32], the tonic excitatory drive computed from EC activity and EC–GC connectivity was applied in parallel to CA3 pyramidal neurons. (7) To test the effects of synaptic heterogeneity (Supplementary Fig. 7), synaptic amplitudes at all synapses were drawn from normal distributions with specified coefficient of variation, CV. Both trial-to-trial (type 1) and synapse-to-synapse (type 2) variability were examined. (8) Finally, to test the effects of heterogeneity in GC excitability (Supplementary Fig. 8), the constant firing threshold (by default 1 in LIF neurons) was replaced by random threshold values for individual cells drawn from a normal distribution with mean 1 and standard deviation σ_{thres}.

Conventions. Throughout the paper, model parameters given in Supplementary Table 1 are referred to as standard parameters. In summary bar graphs, black bars indicate these standard values, light blue bars reduced values, and light red bars increased values in comparison to the default parameter set. In functional analysis of ψ, γ and ρ, standard parameters are indicated as dashed lines. Throughout the paper, the term pattern is defined as a vector of real values (for excitatory drive) or a vector of binary values (for activity, 1 if the cell fires, 0 otherwise). In both cases, the vector length corresponds to the number of cells.

Reporting Summary. Further information on research design is available in the Nature Research Reporting Summary linked to this article.

Data availability

Output datasets can be regenerated from the code[76]. As the full output dataset generated in this work is huge (>10 Tb), deposit in a publicly available repository is not practical at the current time point. Specific data will be provided by the corresponding author on request . Source data are provided with this paper.

Code availability

A minimal version of the Neuron simulation code is provided as Supplementary Software 1. A full version of the simulation and analysis code has been deposited in a publicly available doi-minting repository under the GNU General Public License v.3, as published by the Free Software Foundation[76].

Received: 29 December 2020; Accepted: 12 October 2021;
Published online: 16 December 2021

References

1. Yassa, M. A. & Stark, C. E. Pattern separation in the hippocampus. *Trends Neurosci.* **34**, 515–525 (2011).
2. Rolls, E. T. Pattern separation, completion, and categorisation in the hippocampus and neocortex. *Neurobiol. Learn. Mem.* **129**, 4–28 (2016).
3. Chavlis, S. & Poirazi, P. Pattern separation in the hippocampus through the eyes of computational modeling. *Synapse* **71**, e21972 (2017).
4. Cayco-Gajic, N. A. & Silver, R. A. Re-evaluating circuit mechanisms underlying pattern separation. *Neuron* **101**, 584–602 (2019).
5. Leutgeb, J. K., Leutgeb, S., Moser, M. B. & Moser, E. I. Pattern separation in the dentate gyrus and CA3 of the hippocampus. *Science* **315**, 961–966 (2007).
6. Scharfman, H. E. The dentate gyrus: A comprehensive guide to structure, function, and clinical implications. *Progress Brain Res.* **163**, 627–637 (2007).

7. Bischofberger, J., Engel, D., Frotscher, M. & Jonas, P. Timing and efficacy of transmitter release at mossy fiber synapses in the hippocampal network. *Pflügers Arch.* **453**, 361–372 (2006).
8. Guzman, S. J., Schlögl, A., Frotscher, M. & Jonas, P. Synaptic mechanisms of pattern completion in the hippocampal CA3 network. *Science* **353**, 1117–1123 (2016).
9. Marr, D. A theory of cerebellar cortex. *J. Physiol.* **202**, 437–470 (1969).
10. Albus, J. S. A theory of cerebellar function. *Math. Biosci.* **10**, 25–61 (1971).
11. Amaral, D. G., Ishizuka, N. & Claiborne, B. Neurons, numbers and the hippocampal network. *Prog. Brain Res.* **83**, 1–11 (1990).
12. Boss, B. D., Turlejski, K., Stanfield, B. B. & Cowan, W. M. On the numbers of neurons in fields CA1 and CA3 of the hippocampus of Sprague-Dawley and Wistar rats. *Brain Res.* **406**, 280–287 (1987).
13. Amrein, I., Slomianka, L. & Lipp, H. P. Granule cell number, cell death and cell proliferation in the dentate gyrus of wild-living rodents. *European J. Neurosci.* **20**, 3342–3350 (2004).
14. Coultrip, R., Granger, R. & Lynch, G. A cortical model of winner-take-all competition via lateral inhibition. *Neural Netw.* **5**, 47–54 (1992).
15. Wiechert, M. T., Judkewitz, B., Riecke, H. & Friedrich, R. W. Mechanisms of pattern decorrelation by recurrent neuronal circuits. *Nat. Neurosci.* **13**, 1003–1010 (2010).
16. Papadopoulou, M., Cassenaer, S., Nowotny, T. & Laurent, G. Normalization for sparse encoding of odors by a wide-field interneuron. *Science* **332**, 721–725 (2011).
17. Lin, A. C., Bygrave, A. M., de Calignon, A., Lee, T. & Miesenböck, G. Sparse, decorrelated odor coding in the mushroom body enhances learned odor discrimination. *Nat. Neurosci.* **17**, 559–568 (2014).
18. Maass, W. On the computational power of winner-take-all. *Neural Comput.* **12**, 2519–2535 (2000).
19. de Almeida, L., Idiart, M. & Lisman, J. E. A second function of gamma frequency oscillations: an *E*%-max winner-take-all mechanism selects which cells fire. *J. Neurosci.* **29**, 7497–7503 (2009).
20. Tetzlaff, T., Helias, M., Einevoll, G. T. & Diesmann, M. Decorrelation of neural-network activity by inhibitory feedback. *PLoS Comput. Biol.* **8**, e1002596 (2012).
21. Geiger, J. R. P., Lübke, J., Roth, A., Frotscher, M. & Jonas, P. Submillisecond AMPA receptor-mediated signaling at a principal neuron-interneuron synapse. *Neuron* **18**, 1009–1023 (1997).
22. Espinoza, C., Guzman, S. J., Zhang, X. & Jonas, P. Parvalbumin$^+$ interneurons obey unique connectivity rules and establish a powerful lateral-inhibition microcircuit in dentate gyrus. *Nat. Commun.* **9**, 4605 (2018).
23. O'Reilly, R. C. & McClelland, J. L. Hippocampal conjunctive encoding, storage, and recall: avoiding a trade-off. *Hippocampus* **4**, 661–682 (1994).
24. Neunuebel, J. P. & Knierim, J. J. CA3 retrieves coherent representations from degraded input: direct evidence for CA3 pattern completion and dentate gyrus pattern separation. *Neuron* **81**, 416–427 (2014).
25. Vyleta, N. P., Borges-Merjane, C. & Jonas, P. Plasticity-dependent, full detonation at hippocampal mossy fiber–CA3 pyramidal neuron synapses. *eLife* **5**, e17977 (2016).
26. Cayco-Gajic, N. A., Clopath, C. & Silver, R. A. Sparse synaptic connectivity is required for decorrelation and pattern separation in feedforward networks. *Nat. Commun.* **8**, 1116 (2017).
27. Witter, M. P. The perforant path: projections from the entorhinal cortex to the dentate gyrus. *Prog. Brain Res.* **163**, 43–61 (2007).
28. Bliss, T. V. P. & Lømo, T. Long-lasting potentiation of synaptic transmission in the dentate area of the anaesthetized rabbit following stimulation of the perforant path. *J. Physiol.* **232**, 331–356 (1973).
29. McNaughton, B. L., Douglas, R. M. & Goddard, G. V. Synaptic enhancement in fascia dentata: cooperativity among coactive afferents. *Brain Res.* **157**, 277–293 (1978).
30. McHugh, T. J. et al. Dentate gyrus NMDA receptors mediate rapid pattern separation in the hippocampal network. *Science* **317**, 94–99 (2007).
31. McNaughton, B. L. & Morris, R. G. M. Hippocampal synaptic enhancement and information storage within a distributed memory system. *Trends Neurosci.* **10**, 408–415 (1987).
32. Steward, O. Topographic organization of the projections from the entorhinal area to the hippocampal formation of the rat. *J. Comp. Neurol.* **167**, 285–314 (1976).
33. Zhang, X., Schlögl, A. & Jonas, P. Selective routing of spatial information flow from input to output in hippocampal granule cells. *Neuron* **107**, 1212–1225 (2020).
34. Valiant, L. G. The hippocampus as a stable memory allocator for cortex. *Neural Comput.* **24**, 2873–2899 (2012).
35. Dasgupta, S., Stevens, C. F. & Navlakha, S. A neural algorithm for a fundamental computing problem. *Science* **358**, 793–796 (2017).
36. Sharma J. & Navlakha, S. Improving similarity search with high-dimensional locality-sensitive hashing. Preprint at https://arxiv.org/abs/1812.01844 (2018).
37. Bartos, M. et al. Fast synaptic inhibition promotes synchronized gamma oscillations in hippocampal interneuron networks. *Proc. Natl Acad. Sci. USA* **99**, 13222–13227 (2002).
38. Claiborne, B. J., Amaral, D. G. & Cowan, W. M. A light and electron microscopic analysis of the mossy fibers of the rat dentate gyrus. *J. Comp. Neurol.* **246**, 435–458 (1986).
39. Henze, D. A., Wittner, L. & Buzsáki, G. Single granule cells reliably discharge targets in the hippocampal CA3 network in vivo. *Nat. Neurosci.* **5**, 790–795 (2002).
40. Vandael, D., Borges-Merjane, C., Zhang, X. & Jonas, P. Short-term plasticity at hippocampal mossy fiber synapses is induced by natural activity patterns and associated with vesicle pool engram formation. *Neuron* **107**, 509–521 (2020).
41. Bragin, A. et al. Gamma (40–100 Hz) oscillation in the hippocampus of the behaving rat. *J. Neurosci.* **15**, 47–60 (1995).
42. Pernía-Andrade, A. J. & Jonas, P. Theta-gamma-modulated synaptic currents in hippocampal granule cells in vivo define a mechanism for network oscillations. *Neuron* **81**, 140–152 (2014).
43. Majani, E., Erlanson, R. & Abu-Mostafa, Y. On the *k*-winners takes-all network. *Adv. Neural Inf. Process. Syst.* **1**, 634–642 (1989).
44. Ellias, S. A. & Grossberg, S. Pattern formation, contrast control, and oscillations in the short term memory of shunting on-center off-surround networks. *Biol. Cybern.* **20**, 69–98 (1975).
45. Tamamaki, N. & Nojyo, Y. Projection of the entorhinal layer II neurons in the rat as revealed by intracellular pressure-injection of neurobiotin. *Hippocampus* **3**, 471–480 (1993).
46. Hu, H., Gan, J. & Jonas, P. Fast-spiking, parvalbumin$^+$ GABAergic interneurons: from cellular design to microcircuit function. *Science* **345**, 1255263 (2014).
47. Nörenberg, A., Hu, H., Vida, I., Bartos, M. & Jonas, P. Distinct nonuniform cable properties optimize rapid and efficient activation of fast-spiking GABAergic interneurons. *Proc. Natl Acad. Sci. USA* **107**, 894–899 (2010).
48. Kraushaar, U. & Jonas, P. Efficacy and stability of quantal GABA release at a hippocampal interneuron-principal neuron synapse. *J. Neurosci.* **20**, 5594–5607 (2000).
49. Chamberland, S., Timofeeva, Y., Evstratova, A., Volynski, K. & Tóth, K. Action potential counting at giant mossy fiber terminals gates information transfer in the hippocampus. *Proc. Natl Acad. Sci. USA* **115**, 7434–7439 (2018).
50. Toth, K., Suares, G., Lawrence, J. J., Philips-Tansey, E. & McBain, C. J. Differential mechanisms of transmission at three types of mossy fiber synapse. *J. Neurosci.* **20**, 8279–8289 (2000).
51. LeCun, Y., Bengio, Y. & Hinton, G. Deep learning. *Nature* **521**, 436–444 (2015).
52. Babadi, B. & Sompolinsky, H. Sparseness and expansion in sensory representations. *Neuron* **83**, 1213–1226 (2014).
53. de la Rocha, J., Doiron, B., Shea-Brown, E., Josić, K. & Reyes, A. Correlation between neural spike trains increases with firing rate. *Nature* **448**, 802–806 (2007).
54. Hoeffding, W. Masstabinvariante Korrelationsstheorie. *Schriften Math. Instituts Angew. Math. Univ. Berlin* **5**, 179–233 (1940).
55. Kowalski, J., Gan, J., Jonas, P. & Pernía-Andrade, A. J. Intrinsic membrane properties determine hippocampal differential firing pattern in vivo in anesthetized rats. *Hippocampus* **26**, 668–682 (2016).
56. Engin, E. et al. Tonic inhibitory control of dentate gyrus granule cells by α5-containing $GABA_A$ receptors reduces memory interference. *J. Neurosci.* **35**, 13698–13712 (2015).
57. Espinoza Martinez, C. M. *Parvalbumin$^+$ Interneurons Enable Efficient Pattern Separation in Hippocampal Microcircuits* (IST Austria, 2019); https://doi.org/10.15479/AT:ISTA:6363
58. Braganza, O., Mueller-Komorowska, D., Kelly, T. & Beck, H. Quantitative properties of a feedback circuit predict frequency-dependent pattern separation. *eLife* **9**, e53148 (2020).
59. Bartos, M., Vida, I., Frotscher, M., Geiger, J. R. P. & Jonas, P. Rapid signaling at inhibitory synapses in a dentate gyrus interneuron network. *J. Neurosci.* **21**, 2687–2698 (2001).
60. Hu, H. & Jonas, P. A supercritical density of Na^+ channels ensures fast signaling in GABAergic interneuron axons. *Nat. Neurosci.* **17**, 686–693 (2014).
61. Bucurenciu, I., Kulik, A., Schwaller, B., Frotscher, M. & Jonas, P. Nanodomain coupling between Ca^{2+} channels and Ca^{2+} sensors promotes fast and efficient transmitter release at a cortical GABAergic synapse. *Neuron* **57**, 536–545 (2008).
62. Jones, B. W. et al. Targeted deletion of AKAP7 in dentate granule cells impairs spatial discrimination. *eLife* **5**, e20695 (2016).
63. Pehlevan, C., Sengupta, A. M. & Chklovskii, D. B. Why do similarity matching objectives lead to Hebbian/Anti-Hebbian networks? *Neural Comput.* **30**, 84–124 (2018).
64. Myers, C. E. & Scharfman, H. E. A role for hilar cells in pattern separation in the dentate gyrus: a computational approach. *Hippocampus* **19**, 321–337 (2009).

65. Johnston, S. T., Shtrahman, M., Parylak, S., Gonçalves, J. T. & Gage, F. H. Paradox of pattern separation and adult neurogenesis: A dual role for new neurons balancing memory resolution and robustness. *Neurobiol. Learn. Mem.* **129**, 60–68 (2016).
66. Schneider, C. J., Bezaire, M. & Soltesz, I. Toward a full-scale computational model of the rat dentate gyrus. *Front. Neural Circuits* **6**, 83 (2012).
67. Wang, X. J. & Buzsáki, G. Gamma oscillation by synaptic inhibition in a hippocampal interneuronal network model. *J. Neurosci.***16**, 6402–6413 (1996).
68. Ermentrout, B. Type I membranes, phase resetting curves, and synchrony. *Neural Comput.* **8**, 979–1001 (1996).
69. Carnevale, N. T. & Hines, M. L. *The Neuron Book* (Cambridge Univ. Press, 2006).
70. Schmidt-Hieber, C., Jonas, P. & Bischofberger, J. Subthreshold dendritic signal processing and coincidence detection in dentate gyrus granule cells. *J. Neurosci.* **27**, 8430–8441 (2007).
71. Paxinos, G. & Franklin, K. *The Mouse Brain in Stereotaxic Coordinates* 4th edn (Academic, 2012).
72. Han, Z. S., Buhl, E. H., Lörinczi, Z. & Somogyi, P. A high degree of spatial selectivity in the axonal and dendritic domains of physiologically identified local-circuit neurons in the dentate gyrus of the rat hippocampus. *European J. Neurosci.* **5**, 395–410 (1993).
73. Hefft, S. & Jonas, P. Asynchronous GABA release generates long-lasting inhibition at a hippocampal interneuron-principal neuron synapse. *Nat. Neurosci.* **8**, 1319–1328 (2005).
74. Hosp, J. A. et al. Morpho-physiological criteria divide dentate gyrus interneurons into classes. *Hippocampus* **24**, 189–203 (2014).
75. Armstrong, C. & Soltesz, I. Basket cell dichotomy in microcircuit function. *J. Physiol.* **590**, 683–694 (2012).
76. Guzman, S. J. et al. *Pattern Separation Network* (IST Austria, 2021); https://doi.org/10.15479/AT:ISTA:10110

Acknowledgements

We thank A. Aertsen, N. Kopell, W. Maass, A. Roth, F. Stella and T. Vogels for critically reading earlier versions of the manuscript. We are grateful to F. Marr and C. Altmutter for excellent technical assistance, E. Kralli-Beller for manuscript editing, and the Scientific Service Units of IST Austria for efficient support. Finally, we thank T. Carnevale, L. Erdös, M. Hines, D. Nykamp and D. Schröder for useful discussions, and R. Friedrich and S. Wiechert for sharing unpublished data. This project received funding from the European Research Council (ERC) under the European Union's Horizon 2020 research and innovation programme (grant agreement no. 692692, P.J.) and the Fond zur Förderung der Wissenschaftlichen Forschung (Z 312-B27, Wittgenstein award to P.J. and P 31815 to S.J.G.).

Author contributions

P.J. and S.J.G. designed the model and the layout of the simulations. P.J. and A.S. performed large-scale simulations on computer clusters. C.E., X.Z. and B.A.S. provided experimental data. P.J. and S.J.G. analyzed the data. P.J. wrote the paper and all authors jointly revised it.

Competing interests

The authors declare no competing interests.

Additional information

Extended data is available for this paper at https://doi.org/10.1038/s43588-021-00157-1.

Supplementary information The online version contains supplementary material available at https://doi.org/10.1038/s43588-021-00157-1.

Correspondence and requests for materials should be addressed to Peter Jonas.

Peer review information *Nature Computational Science* thanks Ad Aertsen, Alessandro Treves and the other, anonymous, reviewer(s) for their contribution to the peer review of this work. Handling editor: Ananya Rastogi, in collaboration with the *Nature Computational Science* team.

Reprints and permissions information is available at www.nature.com/reprints.

Publisher's note Springer Nature remains neutral with regard to jurisdictional claims in published maps and institutional affiliations.

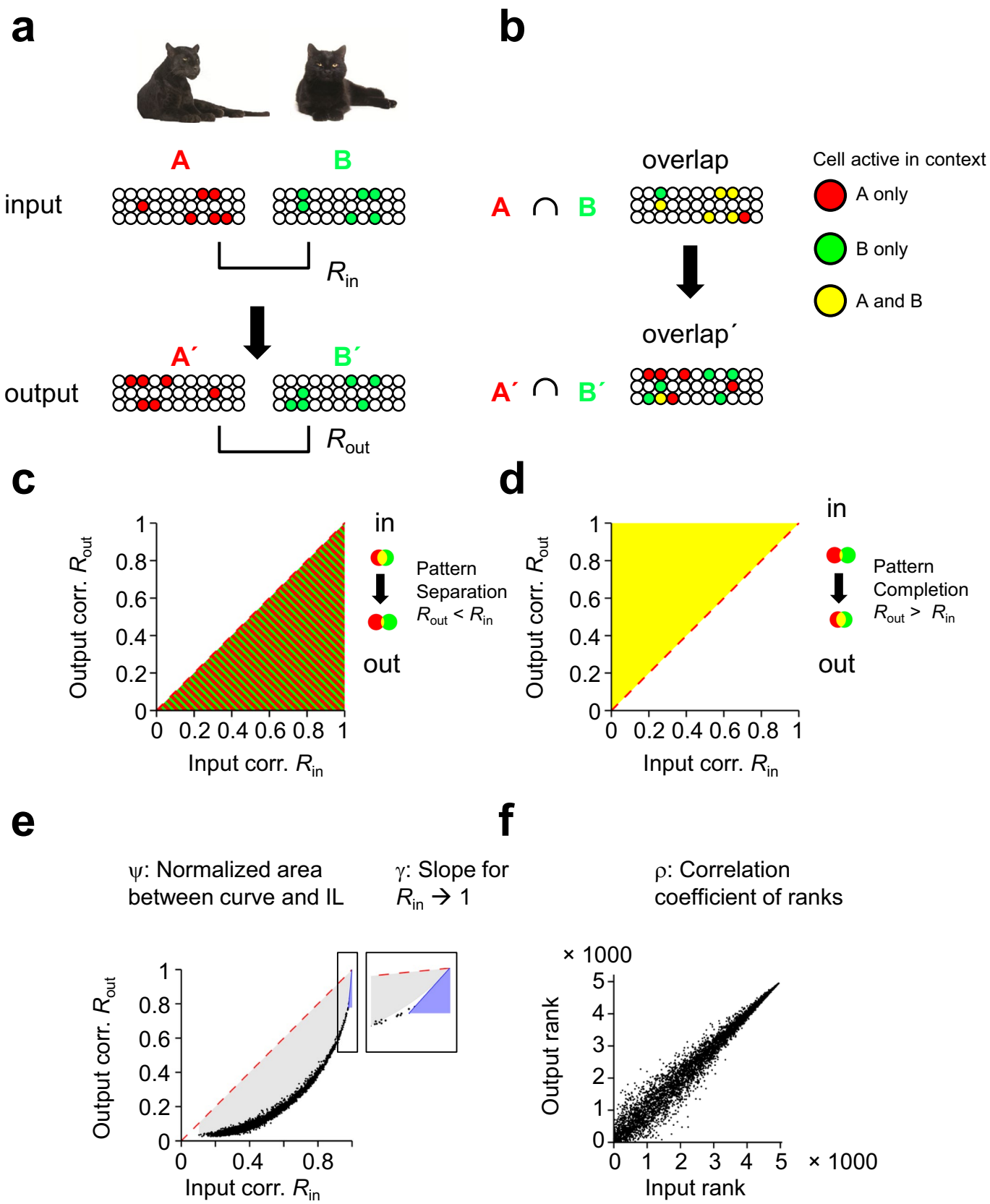

Extended Data Fig. 1 | See next page for caption.

Extended Data Fig. 1 | Quantitative analysis of pattern separation in neuronal networks. a, b, Schematic illustration of pattern separation. (a) Neuronal activity at the input (top) and the output level (bottom) during two similar contexts (top). Red, cells active in pattern A; green, cells active in pattern B; yellow, cells active in both patterns. (b) Overlay of neuronal activity at the input (top) and the output level (bottom). Highly overlapping input patterns (A, B; top) are converted into weakly overlapping output patterns (A′, B′; bottom). Modified from Johnston et al., 2016 (ref. [65]). **c, d**, Analysis of pattern separation and pattern completion in input-output correlation plots (R_{out}–R_{in} graphs). R_{in} and R_{out} represent pairwise correlations in input and output patterns. Red dashed line indicates pattern identity. Area below identity line (red and green stripes, c) represents a regime in which $R_{out} < R_{in}$, that is, pattern separation. Area above identity line (yellow area, d) corresponds to a regime where $R_{out} > R_{in}$, that is, pattern completion. Insets, Venn diagrams of two patterns before and after pattern separation (c) and pattern completion (d). **e, f**, Quantitative analysis of R_{out}–R_{in} graphs. Data points (black points) represent output and input correlations for all pairs of patterns; 4950 data points total. An integral-based metric, ψ, provides a robust assessment of the average pattern separation behavior (e, main panel). ψ was computed as the area between identity line (IL, red dashed line) and the interpolated R_{out}–R_{in} curve (light gray area), normalized to the maximum area (0.5). A slope-based measure, γ, provides a selective analysis of pattern separation in a region of interest in which differences between input patterns are small (e, inset). γ was computed as the slope of the R_{out}–R_{in} curve for $R_{in} \rightarrow 1$. A rank correlation-based measure, ρ, provides an analysis of the ability of the network to preserve rank order similarity (f). ρ was computed as the Pearson's correlation coefficient of the ranks of all R_{out} versus the ranks of all R_{in} data points. R_{out}–R_{in} plot and rank correlation plots are shown for standard model parameters (same data as in Fig. 1c, f; see Supplementary Table 1).

nature research

Corresponding author(s): Peter Jonas

Reporting Summary

Nature Research wishes to improve the reproducibility of the work that we publish. This form provides structure for consistency and transparency in reporting. For further information on Nature Research policies, see Authors & Referees and the Editorial Policy Checklist.

Statistical parameters

When statistical analyses are reported, confirm that the following items are present in the relevant location (e.g. figure legend, table legend, main text, or Methods section).

n/a	Confirmed	
☐	☒	The exact sample size (*n*) for each experimental group/condition, given as a discrete number and unit of measurement
☐	☒	An indication of whether measurements were taken from distinct samples or whether the same sample was measured repeatedly
☐	☒	The statistical test(s) used AND whether they are one- or two-sided *Only common tests should be described solely by name; describe more complex techniques in the Methods section.*
☒	☐	A description of all covariates tested
☐	☒	A description of any assumptions or corrections, such as tests of normality and adjustment for multiple comparisons
☐	☒	A full description of the statistics including central tendency (e.g. means) or other basic estimates (e.g. regression coefficient) AND variation (e.g. standard deviation) or associated estimates of uncertainty (e.g. confidence intervals)
☐	☒	For null hypothesis testing, the test statistic (e.g. *F*, *t*, *r*) with confidence intervals, effect sizes, degrees of freedom and *P* value noted *Give P values as exact values whenever suitable.*
☒	☐	For Bayesian analysis, information on the choice of priors and Markov chain Monte Carlo settings
☒	☐	For hierarchical and complex designs, identification of the appropriate level for tests and full reporting of outcomes
☐	☒	Estimates of effect sizes (e.g. Cohen's *d*, Pearson's *r*), indicating how they were calculated
☐	☒	Clearly defined error bars *State explicitly what error bars represent (e.g. SD, SE, CI)*

Our web collection on statistics for biologists may be useful.

Software and code

Policy information about availability of computer code

Data collection	Simulations of network activity were performed using NEURON version 7.6.2, 7.7.2, or 7.8.2 in combination with Mathematica version 11.3.0.0 or 12.2.0.0 (Wolfram Research). Simulations were tested on reduced-size networks running on a PC using Windows 10. Full-size simulations were run on the IST computer cluster under Debian GNU/Linux version 9 or 10 (https://www.debian.org/), the scheduling system slurm 16.05, the environment module system Lmod 7.7.
Data analysis	Data analysis was performed with Mathematica version 11.3.0.0 or 12.2.0.0 (Wolfram Research) running on a PC using Windows 10.

For manuscripts utilizing custom algorithms or software that are central to the research but not yet described in published literature, software must be made available to editors/reviewers upon request. We strongly encourage code deposition in a community repository (e.g. GitHub). See the Nature Research guidelines for submitting code & software for further information.

Data

Policy information about availability of data

All manuscripts must include a data availability statement. This statement should provide the following information, where applicable:

- Accession codes, unique identifiers, or web links for publicly available datasets
- A list of figures that have associated raw data
- A description of any restrictions on data availability

Source Data for Figures 1–6 and Extended Data Figure 1 are provided with this manuscript. Output data sets can be regenerated from the code (Ref 76). As the full output dataset generated in this work is huge (> 10 Terabyte), deposit in a publicly available repository is not practical at the current time point. Specific data will be provided by the corresponding author upon request (Peter.Jonas@ist.ac.at).

Field-specific reporting

Please select the best fit for your research. If you are not sure, read the appropriate sections before making your selection.

☒ Life sciences ☐ Behavioural & social sciences ☐ Ecological, evolutionary & environmental sciences

For a reference copy of the document with all sections, see nature.com/authors/policies/ReportingSummary-flat.pdf

Life sciences study design

All studies must disclose on these points even when the disclosure is negative.

Sample size	In total, the conclusions in the present paper were based on 784 simulations with the full-scale network model, comprised of 500,000 granule cells, 2,500 interneurons, and 200,000 CA3 pyramidal neurons. Sample sizes were higher than in previous simulation studies. No procedures were used to predetermine sample size. Numbers of neurons were determined by previously published experimental studies (Amrein et al., 2004).
Data exclusions	No data were excluded from the analysis.
Replication	To ensure reproducibility, at the beginning of each simulation, random number generators were initialized with defined seeds. Attempts at replication were always successful and gave identical results. In addition, Simulations with 5 different seeds gave very similar results for the standard parameter settings.
Randomization	Simulations were allocated into groups according to parameter value settings. Thus, randomization was not relevant to your study.
Blinding	Simulations were run with precisely defined parameter value settings. Thus, blinding was not applicable to our study.

Reporting for specific materials, systems and methods

Materials & experimental systems

n/a	Involved in the study
☒	☐ Unique biological materials
☒	☐ Antibodies
☒	☐ Eukaryotic cell lines
☒	☐ Palaeontology
☒	☐ Animals and other organisms
☒	☐ Human research participants

Methods

n/a	Involved in the study
☒	☐ ChIP-seq
☒	☐ Flow cytometry
☒	☐ MRI-based neuroimaging